RESEARCH ARTICLE

NANO · MICRO small
www.small-journal.com

Tungsten Strongly Inhibits Sintering of Porous Iron During High-Temperature Redox Cycling

Samuel Pennell, Ming Chen, and David C. Dunand**

Freeze-cast Fe-25 W (at%) lamellar foams show excellent resistance to degradation at 800 °C during steam-hydrogen redox cycling between the metallic and oxide states, with fast reaction kinetics maintained up to at least 100 redox cycles with full Fe utilization. This very high stability stems from the sintering inhibition of W combined with the freeze-cast architecture and the chemical vapor transport (CVT) mechanism of reduction. These three factors create a hierarchical porosity in the foam, consisting of i) macroscopic elongated channels, ii) micro-scale sintering inhibition pores, and iii) submicron CVT pores. Microstructural characterization via SEM and EDS is combined with in situ XRD to fully explore the phase evolution and microstructural impact of W on Fe during redox cycling. Comparison with tapped Fe-25 W (at%) powder beds reveals that the freeze-cast channels and lamellae are not critical to the performance of the material.

1. Introduction

Iron is an attractive energy-storage material due to its abundance, low cost, and nontoxicity. At high temperatures, iron can be oxidized by steam, and its oxides can be reduced by hydrogen, making iron a viable energy-storage material for the nascent rechargeable oxide battery (ROB) space.[1,2] The ROB devices utilize the energy-storage material to convert a fixed amount of steam into hydrogen which is then fed into a connected reversible solid oxide cell. Similar gas-conversion technologies could use iron as a prospective, low-cost utility material, such as i) chemical looping combustion, wherein the iron oxide is reduced by fuel such as CH_4, followed by a re-oxidation in air to produce heat,[3–6] ii) carbon utilization, wherein CO_2 oxidizes Fe to produce CO as a chemical feedstock (e.g., for acetic acid), resulting in carbon sequestration and value-added CO_2 use,[7–9] or iii) solar thermal redox, where extreme temperatures cause thermal reduction.[10,11] All these technologies rely on the ability of the cycling material (e.g., iron) to convert from metal to oxide and vice versa while maintaining the same reactivity over multiple redox cycles and completing each half cycle in a practical timescale.

While beds of pure Fe powders show promise during the first few redox cycles at the high temperatures (above 700 °C) necessary to achieve fast kinetics, they quickly lose reactivity due to powder sintering in both the metallic (T_m = 1538 °C) and oxide Fe_3O_4 (T_m = 1597 °C) states.[12] Sintering greatly slows redox kinetics by i) reducing the active surface area of the material via densification of the powders within the bed and ii) blocking gas access to the metal powders via the formation of a dense layer on the outer surface of the powder bed.[12–14]

Several strategies have been used to address this sintering-induced degradation. Frequently, the iron material is supported on an inactive oxide material such as titania, alumina, zirconia, or Mg-Al-O spinel.[15–20] The underlying oxide support acts as a barrier to diffusion and sintering by preventing contact between nearby iron particles. The impact of porosity in these systems is key, as the materials with the best long-term performance, such as the $FeTiO_3$ materials investigated by Chung et al., show stable or even increasing porosity with continued cycling, rather than densification of pores.[20,21]

Alloying iron with other metals is another strategy, with the candidate additions falling into three categories: inactive metals, inactive oxides, or redox-active metals.[22] Inactive metals – such as Ni and Cu – are not oxidized by steam under standard redox conditions, and instead provide a mechanically stable, metallic backbone during cycling.[23] The interface between the metallic backbone and the iron oxide layer forming during oxidation helps accelerate reduction kinetics.[24,25] For Fe-soluble inactive metals like Ni, the backbone provides a sink for Fe during reduction which helps stabilize the microstructure.[24] Metals such as Al or Cr oxidize under steam into stable oxides which are not reduced by H_2, effectively turning the alloy into the inactive oxide case discussed above.[23]

Redox-active metals comprise two main members, Mo and W. These refractory metals have very high melting points and thus provide sintering inhibition similar to that seen for oxide supports, while also contributing to the redox activity of the material. Our previous study of Fe—Mo redox cycling shows that

---

S. Pennell, M. Chen, D. C. Dunand
Department of Materials Science & Engineering
Northwestern University
Evanston, IL 60208, USA
E-mail: samuelpennell2024@u.northwestern.edu;
dunand@northwestern.edu

The ORCID identification number(s) for the author(s) of this article can be found under https://doi.org/10.1002/smll.202402174

DOI: 10.1002/smll.202402174

Mo strongly inhibits degradation by sintering as compared to Fe-Ni.[26] Some degradation remains however: i) Mo-rich phases segregate away from the surface of the microstructure as redox cycles are accumulated, and Mo loses its beneficial impact on the remaining Fe, and ii) volatilization of $MoO_2(OH)_2$ causes further loss of Mo from the material due to chemical vapor transport.[26,27]

While initially observed to be detrimental to cycling characteristics by Ostuka et al.,[22] W has recently been shown to have a positive impact on the stability of iron undergoing high-temperature redox cycling in different gas environments: Morales-Corona et al. showed that 5–40 mg samples of Fe powders alloyed 2 or 5 at% W showed good structural stability when redox-cycled at 850 °C in a fluidized bed reactor (reduced with N_2-15%CO and oxidized with N_2-4%O_2), and that the W helped mitigate agglomeration and carbon deposition.[28] Liu et al. examined $FeWO_x$ / SiO_2 (60 wt.% SiO_2) nanopowders for the production of syngas (reduced with N_2-10% CH_4, oxidized with air), where again W addition aided the structural stability and reactivity of the system.[29] However, a detailed examination of the microstructural evolution of high W-content Fe-W materials has not yet been conducted, nor has there been a study of this material under H_2/H_2O cycling. Further, the use of micron- rather than nano-size powders in foams with a mass of ≈1 g is of practical interest and can strongly affect the structure and agglomeration of the powders.

Any of these composition-based strategies can be combined with a structural approach besides a simple powder bed; for example, 3-D architectures (such as ink-printed lattices, extruded grates, and freeze-cast foams) can provide a pore structure that lowers tortuosity, so that gas can easily enter and escape the reacting material.[30,31] Our previous work with directionally freeze-cast foams shows that the directional channels and low tortuosity are effective for solid–gas reactions.[32–34] Additionally, freeze casting is a low-cost manufacturing method that provides a very fine pore structure, with channel widths as narrow as 20 µm.[32,35,36] This is sufficiently wide to provide low tortuosity for hydrogen and steam, without allocating excessive foam volume to pores. However, freeze-cast foams undergo a unique degradation mechanism: due to the high aspect ratio of the lamellae, buckling is easily induced by the high stresses due to cyclic expansion and contraction during oxidation and reduction, respectively. For foams without a sintering inhibitor, sintering and densification occur due to contact between neighboring lamellae that buckle and contact each other, eliminating the benefits of the foam architecture.[24,30,34]

Here, we show extreme degradation resistance of Fe-25 W (at%) freeze-cast foams during high-temperature redox cycling. This composition was chosen to form continuous phases of Fe_2W and $FeWO_4$ in the material, allowing for a detailed examination of the effects of the two-phase microstructure as shown in our previous studies with the same content of Ni, Co, and Mo.[24,26,30] This relatively high W content also serves as a useful point of comparison for future studies of lower W content. The degradation resistance of this material stems from both the sintering inhibition inherent to W and the nature of the intermetallic and mixed oxide compounds formed between Fe and W, such that W does not segregate, and remains atomically mixed with Fe at all times, unlike previously studied Fe—Mo foams.[26] The Fe—W foams show good redox kinetics over long-term cycling: they fully oxidize and reduce within 90 min after 100 full cycles, with no segregation of W or densification of the foam observed.

2. Results and Discussion

2.1. Thermodynamic Considerations

The isothermal (800 °C) section of the Fe—W—O ternary phase diagram is shown in **Figure 1**. At this temperature, the fully reduced Fe-25 W foam is expected to consist of an equimolar mixture of two phases: bcc α–Fe(1.3 W) and λ–Fe_2W. During oxidation by H_2O, this mixture approaches the Fe_3O_4 – $FeWO_4$ two-phase region in the ternary phase diagram (Figure 1a, blue arrow), first moving into a three-phase Fe—Fe_2W—$FeWO_4$ region, followed by a FeO—Fe_3O_4—$FeWO_4$ region, and finally the two-phase Fe_3O_4—$FeWO_4$ region (Figure 1a, green line). Further oxidation with steam to form Fe_2O_3 is not possible under ambient pressure conditions.[37] During H_2 reduction, oxygen is removed from the system as H_2O, and the phase evolution proceeds in reverse, returning to the initial equimolar Fe+Fe_2W composition.

While the ternary phase diagram describes oxygen additions to the Fe-25 W composition accurately, the use of steam as an oxidizing agent and hydrogen as a reduction agent brings additional thermodynamic considerations. The Baur–Glässner diagram is a useful tool showing phase stability as a function of the H_2/H_2O ratio and temperature. Oxidation reactions that require pure (or nearly pure) H_2O, and reduction reactions that require pure (or nearly pure) H_2 are not practical for use in rechargeable oxide batteries, since the energy storage material is expected to be exposed to a mixture of both gases. Figure 1b shows the Baur–Glässner diagram for the Fe system (black, blue, and green lines), with the first reaction of the Fe-25 W system (purple line for $Fe_2W + Fe \leftrightarrow FeWO_4 + Fe$) superposed, based on experimentally-determined thermodynamic energies.[38–40] The diagram indicates that, while $FeWO_4$ is more stable than Fe_3O_4, it is not so stable that pure H_2 is necessary for its reduction at 800 °C (in fact, an H_2/H_2O ratio of 2.8 is sufficient at 800 °C). After formation of $FeWO_4$, further oxidation of Fe to FeO and Fe_3O_4 follows the same path as for pure Fe, since all W has been converted to $FeWO_4$. This is corroborated by the conversion of the Baur–Glaessner diagram to equivalent oxygen partial pressure, shown in Figure 1c. A suitable energy-storage material should have its lower and upper oxidation state equilibrium lines lie between those for a 4:1 and 1:4 mixture of H_2/H_2O (Figure 1c, red dashed lines), taken as values that can be easily achieved in battery operation. The oxygen partial pressure p_{O2} values for $Fe_2W/FeWO_4$ (purple line) closely approach those for Fe_3O_4/FeO (green line) at 1073 K, indicating that the W addition does not reduce the suitability of the Fe redox system from a thermodynamic perspective. Using the Nernst equation for high-temperature fuel cells, these p_{O2} values give a Nernst potential of 0.92 V for the Fe-25 W alloy, slightly lower than the 0.94 V value determined for the pure Fe system.[41]

2.2. Initial Structure

To provide sufficient mechanical strength to the foam so they are not damaged during handling, sintering is performed at a much

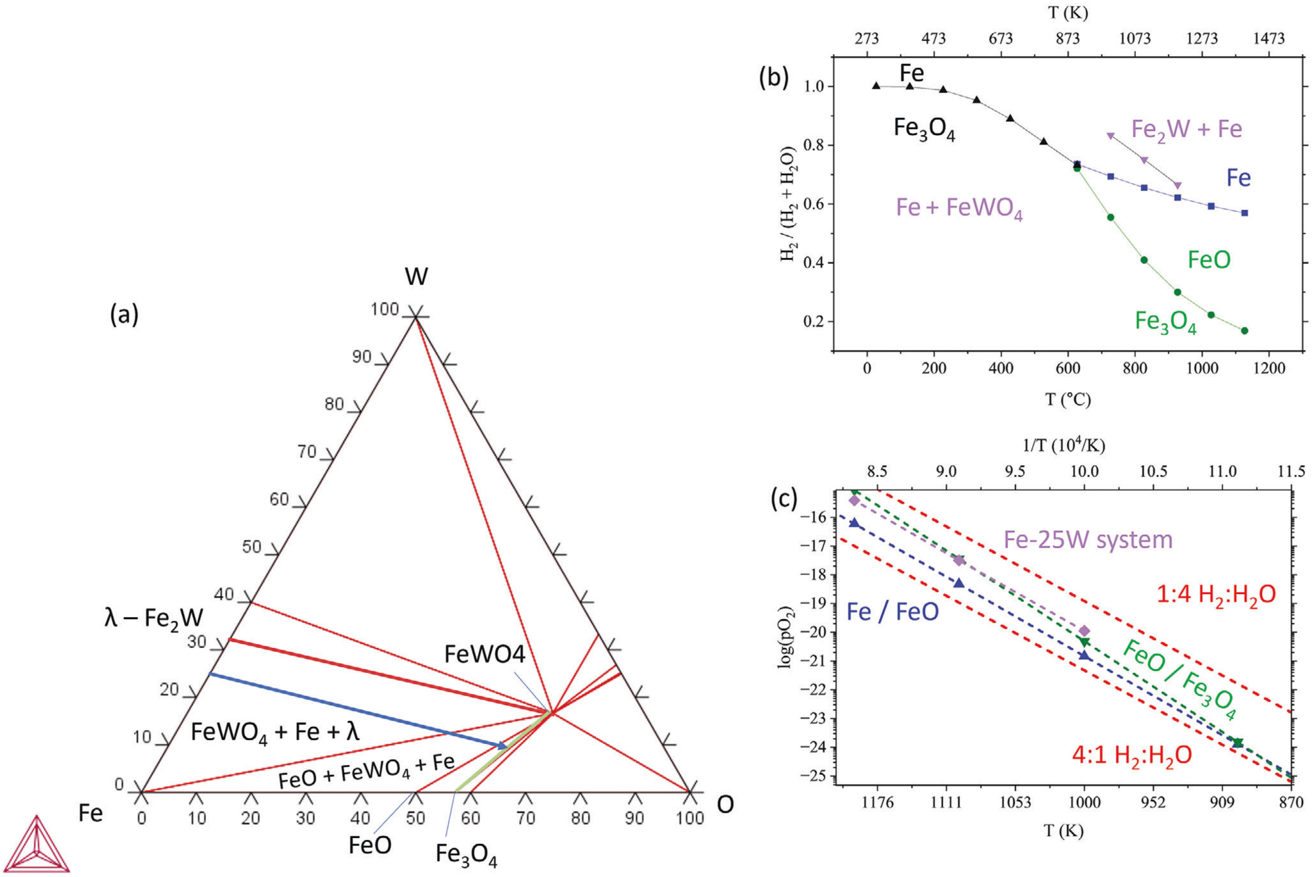

Figure 1. a) isothermal section of the Fe—W—O ternary phase diagram at 800 °C. The blue arrow indicates the overall phase evolution path for the Fe-25 W alloy atomic ratio Fe:W = 3, and the green phase boundary (Fe_3O_4—$FeWO_4$) indicates the fully oxidized composition. b) Baur–Glässner diagram showing expected phase formation as a function of temperature and H_2 partial pressure. In addition to Fe, FeO, and Fe_3O_4, thermodynamic data for the Fe-25 W system are added in purple for comparison. c) Arrhenius plot showing the various redox couples as a function of temperature and oxygen partial pressure (pO_2). Feasible systems should fall within the 1:4 and 4:1 H_2:H_2O boundaries (red dotted lines); the Fe-25 W system meets these criteria.

higher temperature (1200 °C) than redox cycling (800 °C). As a result, the initial phase composition is different than that achieved during cycling. After reduction and sintering at 1200 °C, each lamella in the foam consists of a mixture of bcc α-Fe (with ≈1 at% in solid solution) and μ–Fe_7W_6, as predicted by the Fe—W phase diagram. During oxidation (the first half cycle), α-Fe oxidizes to Fe_3O_4 and μ-Fe_7W_6 oxidizes to $FeWO_4$ and minor amounts of Fe_3O_4. The subsequent reduction of these two oxide phases at 800 °C does not return the foam to its initial phases (reached at 1200 °C); rather, the 800 °C equilibrium phases are reached: bcc α-Fe (with 1.3 W in solid solution) and λ-Fe_2W. During reduction, the Fe_3O_4 reduces back to bcc Fe, and the $FeWO_4$ reduces more slowly to Fe_2W. Because there is a mismatch in the stoichiometric ratio between Fe and W in moving from $FeWO_4$ (Fe:W = 1) to Fe_2W (Fe:W = 2), Fe from the surrounding matrix (from the prior reduction of Fe_3O_4) is used to form the intermetallic Fe_2W.

Reduction of Fe_3O_4 powders is well described by the shrinking-core model, where the reducing gas (H_2) dissociates and absorbs into vacancies in the oxide surface, before reacting with oxygen anions supplied from Fe_3O_4 to form H_2O and Fe cations, with charge balance maintained by the donation of electrons from the oxygen anion.[42] The H_2O molecule then desorbs while the Fe ions and electrons migrate to the internal Fe_3O_4 / FeO interface to form FeO.[42] While the first $Fe_3O_4 \rightarrow FeO$ reduction is dependent on the inward diffusion of Fe ions, the subsequent $FeO \rightarrow Fe$ reduction relies on the outward diffusion of oxygen anions through the outer metallic Fe layer to the gas interface; as the Fe layer grows, the diffusion distance increases, thus slowing the reaction kinetics.[42–44] Short-circuit diffusion via cracks, pores, or grain boundaries can however improve kinetics.[42] In the Fe-25 W foams studied here, the high internal porosity of each lamella provides unobstructed gas access to each micron-scale Fe_3O_4 region, with diffusion distances being greatly shortened as compared to larger, dense Fe particles.

The mechanism of $FeWO_4$ reduction, however, is different from that of Fe_3O_4: at high temperatures and in the presence of H_2, $FeWO_4$ may be reduced by a chemical vapor transport (CVT) mechanism, as also observed for hydrogen reduction of WO_3 and WO_2.[45,46] The observation of CVT for WO_x reduction implies that the mixed oxide $FeWO_4$ must undergo a transient state where the WO_x content drops because of CVT, and the FeO_{4-x} content decreases via the shrinking core mechanism. Despite this, no pure W phase is observed during reduction (as observed via XRD and EDS), only the equilibrium λ-Fe_2W phase. Thus, it

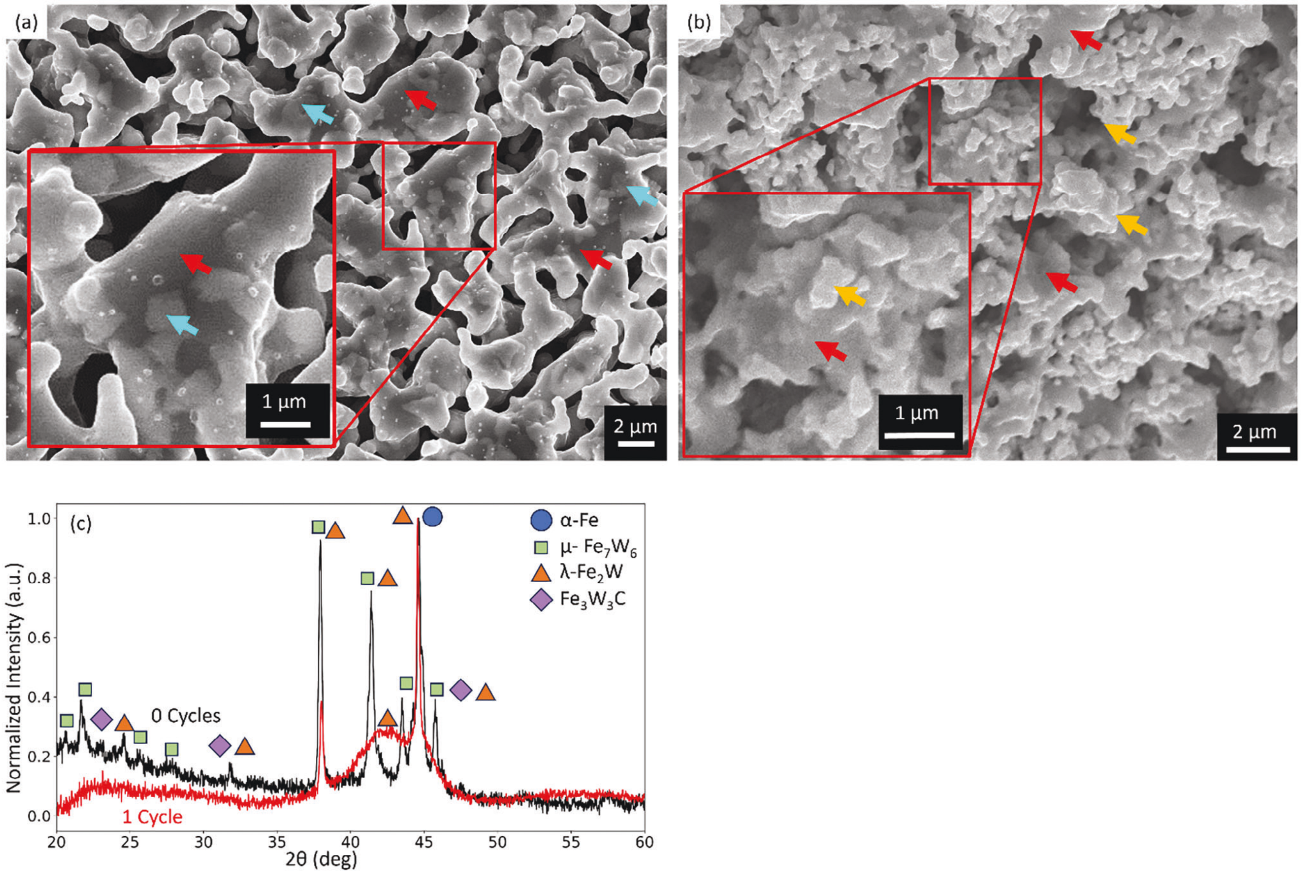

Figure 2. SEM micrographs of the surface of a representative lamella in a Fe-25 W foam a) after initial reduction and sintering at 1200 °C and b) after one redox cycle at 800 °C. Blue arrows indicate μ-Fe_7W_6, red arrows indicate α–Fe, and yellow arrows indicate λ–Fe_2W, as determined by Z-contrast, with overall composition confirmed by XRD. c) XRD spectra of Fe-25 W freeze cast foams after initial reduction and sintering at 1200 °C (black) and after the first redox cycle at 800 °C (red). Before cycling, the foam consists of a mixture of crystalline α-Fe (blue circle) and μ-Fe_7W_6 (green square), with some residual Fe_3W_3C carbide (purple diamond) from binder burnout. After cycling, the foam is returned to the equilibrium phases at 800 °C: α-Fe and λ-Fe_2W (orange triangle), with the carbide removed by carbon oxidation. The broad hump between 40 and 48° is indicative of nano-crystalline λ-Fe_2W formed by CVT reduction.

appears that, while some pure W may initially form due to the CVT reduction of binary WO_x, it reacts with nearby Fe to form the binary λ-Fe_2W phase. The absence of metallic W from XRD and EDS measurements does not preclude that small amounts of transient W form, below the detection limit, and react to λ-Fe_2W.

The main consequence of the CVT reduction hypothesis is that reduced λ-Fe_2W will be nanocrystalline, with submicron pores present between the nascent Fe_2W nano-grains. The CVT mechanism is consistent with the microstructure of the lamellae before (**Figure** 2a) and after (Figure 2b) the first reduction half cycle at 800 °C, and the corresponding XRD patterns are shown in Figure 2. Red arrows mark α-Fe (with some W in solid solution), blue arrows mark μ-Fe_7W_6 before the first cycle, and yellow arrows mark λ-Fe_2W after the first cycle, as determined by backscatter electron Z-contrast in conjunction with XRD patterns. The XRD patterns (Figure 2c) confirm that the λ-Fe_2W phase is nanocrystalline (as shown by the broad shoulder), as well as highly textured, as the peak at diffraction angle $2\theta = 38°$ is relatively narrow compared to the broad nanocrystalline peaks between 40 and 48°. Additionally, a small amount of ternary carbide (Fe_3W_3C) is initially present, formed from the reaction between the organic binder and the foam during burnout, but this carbon is removed by oxidation to CO/CO_2 during the first oxidation half-cycle.

This nano-porous and nanograin microstructure provides a further boost to the kinetics of subsequent redox cycles, as the slower-reacting W-rich phase is nanometric, increasing its kinetics of oxidation and reduction. The submicron pores also provide a greater degree of gas access to the foam, thus lowering solid-state diffusion distances to submicron levels. After the foam phases equilibrate in the first cycle, subsequent redox cycling is expected to follow the following reversible reaction:

$$Fe + Fe_2W + \frac{20}{3}H_2O \leftrightarrow FeWO_4 + \frac{2}{3}Fe_3O_4 + \frac{20}{3}H_2 \tag{1}$$

proceeding forward under steam oxidation and in reverse under hydrogen reduction. A crucial consequence of this reaction sequence is that W is always found in a compound with Fe, and no Fe-free W or WO_x compounds are expected to form.

After the first cycle, the foam consists of three levels of pore size, as shown schematically in **Figure** 3a, and in micrographs in

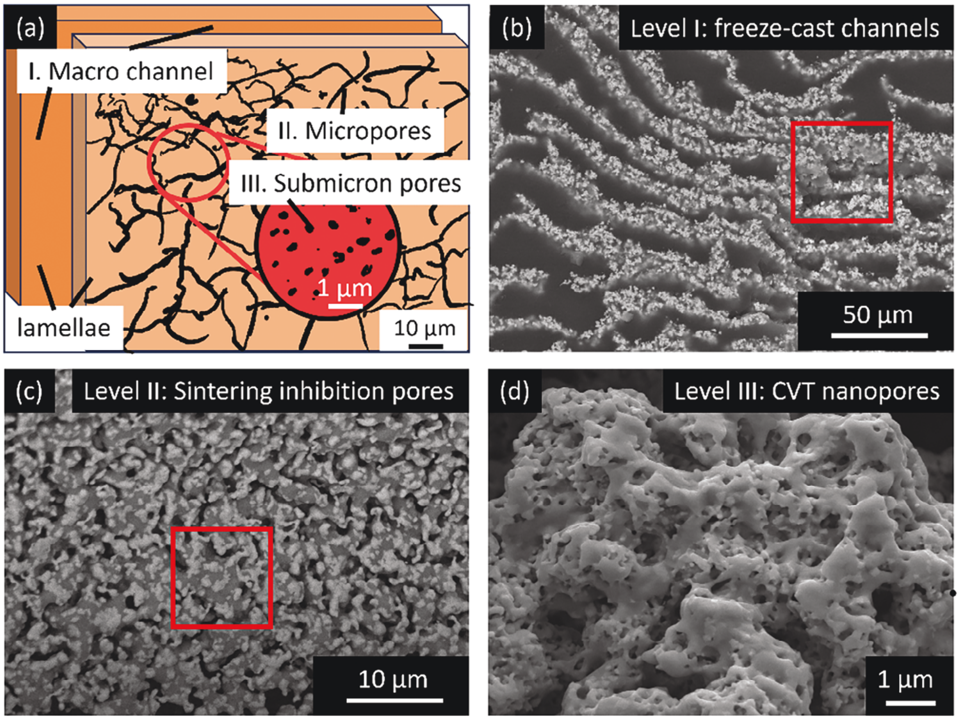

Figure 3. a) schematic depiction of the three hierarchical levels of porosity present in the foams, with inset (black circle) showing schematically the submicron pores. b–d) Micrographs illustrating the hierarchical porosity present in reduced Fe-25 W foams after the first cycle consisting of three levels: b) level I – macroscopic freeze cast channels, shown in a radial cross-section micrograph, c) level II – microscale sintering-inhibition pore network, shown in surface electron image, and d) level III – submicron CVT nanopores, shown in surface electron image. For illustration, the size of the micrographs (c) and (d) are illustrated as red boxes in (b) and (c), respectively.

Figure 2b–d: (level I) macroscopic freeze-cast channels, ≈20 µm in width and running the full height (12 mm) of the foam, separating lamellae which are distributed into colonies with aligned radial orientation; (level II) microscale sintering-inhibition pore network within each lamella, fully continuous, formed due to the sintering inhibition of W; (level III) submicron CVT pores, formed within each W-containing area in the lamellae, regenerated at each reduction half-cycle. The retention of these three levels of porosity is key for the prolonged cycling stability of the foam, as this pore hierarchy provides excellent gas access to all parts of the foam, minimizing the reaction time needed to fully oxidize or reduce it.

2.3. Phase and Microstructural Evolution of Freeze-Cast Foams During Redox Cycling

2.3.1. Phase Evolution

To confirm the expected phase evolution and compare the kinetics of oxidation and reduction of these various phases, in situ X-ray diffraction was performed on lamellae cut from the full freeze cast foams; to slow the reaction kinetics for better time resolution, flow rates of Ar and H_2 were lowered to 60 sccm, and Ar-4% H_2 was used as the reducing gas, rather than H_2. As a result, while the in situ XRD result trends are applicable to the bulk foam redox behavior, the precise cycling times for bulk foams are not directly measured by in situ XRD.

Waterfall XRD spectra of the first two cycles are shown in **Figure 4**a, with diffraction peaks labeled. The corresponding normalized peak intensities, calculated from the peak area of the strongest, nonoverlapping peak for each species, for each cycle, are shown in Figure 4; each peak is normalized against its own greatest value, rather than against the overall maximum value to better observe the evolution of each phase individually.

At the beginning of the first redox cycle, the alloy consists of α-Fe (with 1.3% W in solid solution) and µ-Fe_7W_6. During oxidation, $FeWO_4$ forms first, followed by Fe_3O_4 after 10 min. This oxidation cascade from Fe to FeO to Fe_3O_4 is relatively rapid, with completion taking 20 min after the initial Fe_3O_4 is formed. The W oxidation rate is however slower (65 min); the discrepancy in oxidation rates leads to the formation of a bcc-W phase between 20 and 70 min, which then slowly oxidizes to $FeWO_4$. During the subsequent reduction, Fe_3O_4 reacts faster, reducing back to Fe in 25 min. By contrast, $FeWO_4$ reduces more slowly, and the final composition consists of α-Fe and λ-Fe_2W. The reduced Fe_2W is nanocrystalline (as discussed previously), and the corresponding diffraction peaks are very broad. As a result, the broadened peak region overlaps with the sharp crystalline peaks for W and FeO; the normalized peak integrals for these two phases were masked during data processing so that erroneous peak identification is avoided.

After the first redox cycle, the reaction kinetics are greatly accelerated. This is attributed to two factors: i) the microstructure, altered by the CVT reduction mechanism, has a much higher surface area due to submicron pore formation, and ii) the Fe_2W

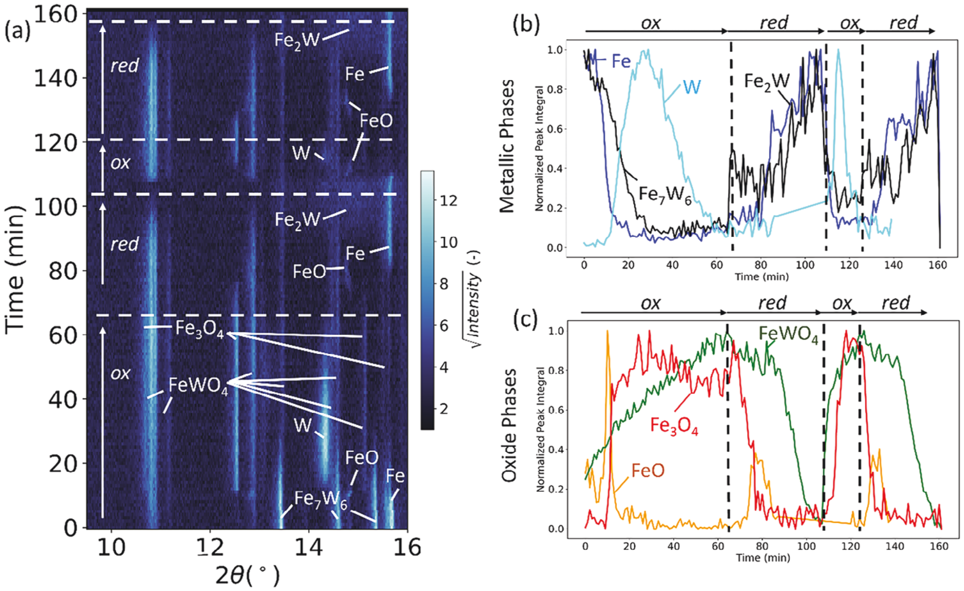

Figure 4. In situ XRD results for Fe-25 W foam during the first two redox cycles. a) waterfall diffractograms as a function of time for the full two-cycle process, with phases and reduction ("red") and oxidation ("ox") reactions indicated. b) the plot of the evolution of normalized peak height integrals for metallic phases during the first and second cycles c) plot of the evolution of normalized peak integrals for oxide phases during the first and second cycles.

phase oxidizes more rapidly than Fe_7W_6 and does not form a large amount of transient W phase during oxidation. In the second cycle, the oxidation rate is slightly faster for $FeWO_4$ than for Fe_3O_4, and both proceed much more rapidly than in the first cycle, with oxidation complete after 15 min (compared to 68 min in the first cycle). During reduction, Fe_3O_4 reduces first, followed, after 20 min, by reduction of the more stable $FeWO_4$, though the reduction rate is similar for both species. The total reduction time of the second cycle is 25 min, compared to 40 min in the first cycle. After reduction, the Fe_2W + Fe phase composition is recovered.

Replicate testing across four additional foams showed that the second oxidation was, on average, 55% (±13%) faster than the first oxidation, and the second reduction was, on average, 31% (±19%) faster than the first reduction. All replicates showed the same trend of pure W formation during the first oxidation and much lower amount of pure W formation in the second oxidation.

2.3.2. Microstructural Evolution

The microstructure of foams after 1, 10, 20, 50, and 100 cycles is shown in **Figure 5** in cross-section micrographs in the reduced (left) and oxidized (right) states. In the reduced state, each lamella consists of 2–5 µm ligaments interpenetrated by open porosity (red arrows) of the same size. Each ligament, in turn, consists of an interpenetrating network of α-Fe (with 1.3% W in solid solution) submicron λ-Fe_2W grains, and submicron CVT pores. This same reduced microstructure is maintained through 50 cycles with the microscale porosity increasing as cycling progresses. Since each reduction and oxidation half-cycle fully reduced or oxidized the Fe and W, these cycles represent 100% Fe utilization.

The oxidized state consists of two interpenetrating networks of Fe_3O_4 and $FeWO_4$. Between 1 and 10 cycles (Figure 5b,d), this double network fills most of the microporosity present in the lamellae, but as cycling progresses to 20 cycles (Figure 5f) and beyond, the volume fraction of microporosity increases and the oxide expansion no longer fills all the porosity available in the lamellae. Simultaneously, the $FeWO_4$ domain size (green arrows), which is initially large (up to 10 µm), decreases with cycling as the CVT mechanism redistributes W within the lamellae. After 20, 50, and 100 cycles, the oxidized microstructure closely resembles that of the reduced microstructure, albeit without the submicron CVT pores which are always filled by volume expansion during oxidation, then re-created during the subsequent reduction.

The increase in microporosity observed after more extensive cycling is accompanied by a drop in the domain size of each oxide. After the first cycle, the Fe_3O_4 and $FeWO_4$ domains are ≈10 µm in size, with minimal interpenetration between neighboring areas. After ten cycles, mixing has improved, and the still-distinct domains are ≈2–3 µm in size. After 20 cycles (Figure 5f), and further after 50 and 100 cycles (Figure 5h,i), the domains are ≈1 µm in size, and the $FeWO_4$ domains are evenly distributed within a Fe_3O_4 matrix rather than segregated in larger regions. Phase composition is confirmed by XRD analysis, and discussed below.

Remarkably, the oxidized state micrographs indicate that, with increasing cycling numbers, individual lamellae become more porous rather than denser, as would be expected for a high-temperature process due to sintering, and as was observed in previous studies of Fe—Ni, Fe—Cu, and Fe—Co redox systems.[24,30,33,47] Also, the phases become more homogeneously mixed rather than more segregated, as also observed in these other systems. The initially higher density of the lamellae is attributed to the high sintering temperature of 1200 °C. During

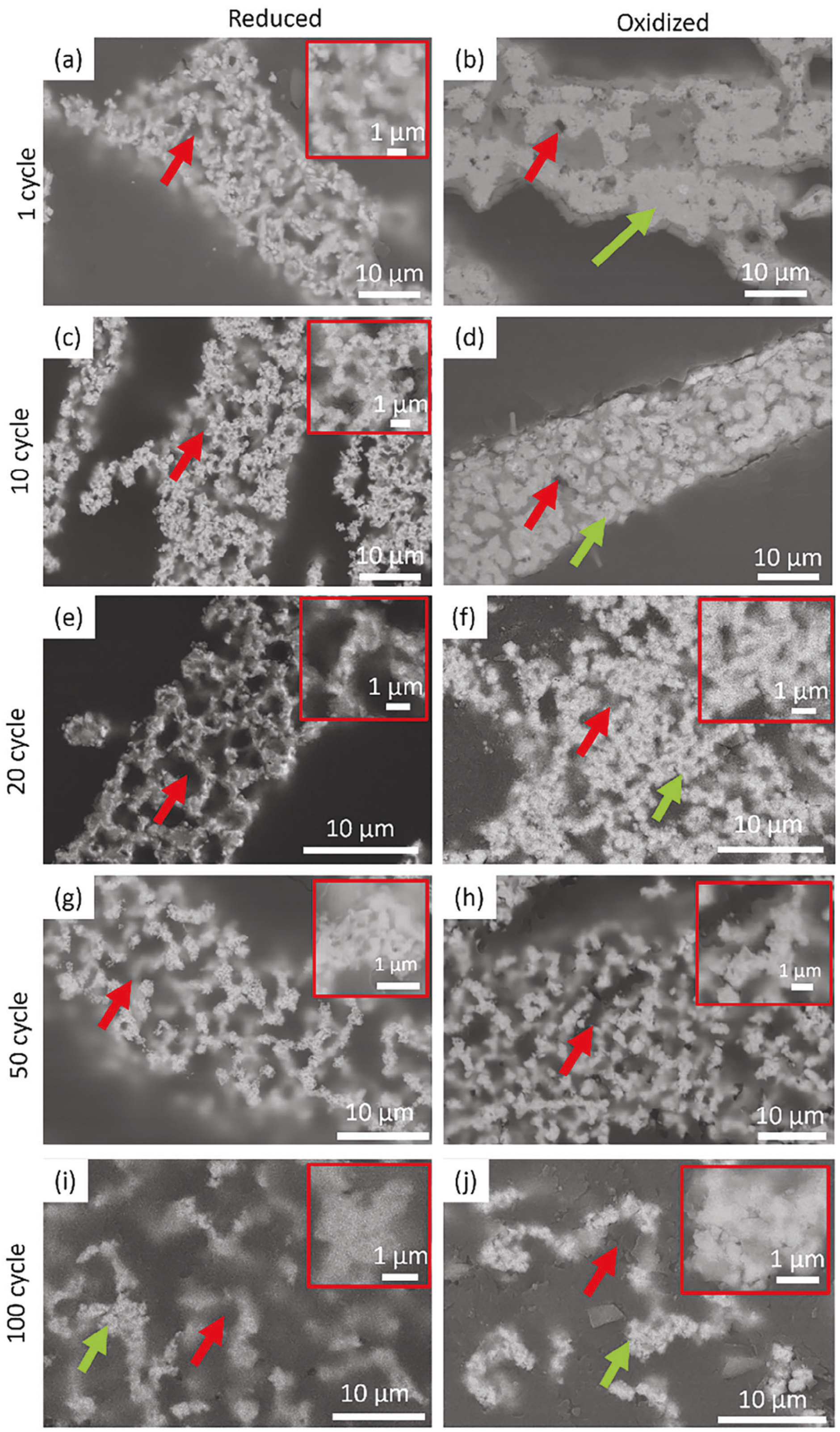

Figure 5. Radial cross-section SEM micrographs showing microstructural evolution for Fe-25 W foams after 1, 10, 20, 50, and 100 redox cycles at 800 °C, in the reduced state (left column) and the oxidized state (right column). Red arrows mark micropores, and green arrows mark W-containing phases (Fe_2W for the reduced state, $FeWO_4$ for the oxidized state).

cycling, the lower cycling temperature of 800 °C is insufficient to induce further sintering in the W-rich phases (Fe_2W and $FeWO_4$). Additionally, the high volume fraction of these phases, combined with the cyclic regeneration of submicron pores by CVT reduction, is sufficient to open new submicron pores that did not initially exist in the as-sintered foam and to homogenize the size and shape of both new and existing pores. The CVT reduction also serves to break up the initially unmixed $FeWO_4$ regions and redistribute their W content throughout the lamella, leading to an increasingly dispersed microstructure that is expected to be more reactive, due to shorter diffusion distances and increased interfacial area. In addition to new submicron pores forming during cycling, the microscale sintering inhibition pores grow in size due to the escape of steam during reduction. The formation of pores during hydrogen reduction is well known from the production of sponge iron,[24,42] and in the Fe-25 W foams these pores do not sinter closed, leading to an increase in pore volume fraction with continued cycling.

The major degradation mechanisms (Fe-shell formation and aggregation of the alloying element) observed in previously studied Fe-X redox cycling materials are absent. No shell is observed to form at the edges of the lamellae or at the edges of the foam overall, and no W coarsening is observed. This is probably because, unlike the Fe-25Mo system where MoO_2 is formed each cycle, no binary WO_2 is observed.[26] Instead, all W content is oxidized to the ternary $FeWO_4$ phase, resulting in the atomic mixing of W and Fe in both the oxidized and reduced states.

The conclusions drawn from the cross-sectional microstructure are supported by the microstructure of foam surfaces (unsanctioned) as well, with representative micrographs after 1, 10, 20, 50, and 100 cycles shown in **Figure 6**. Initially, the reduced surface contains two levels of porosity: micro-scale, sintering-inhibition pores, and submicron CVT pores (Figure 6a). The corresponding oxidation fills much of this porosity, though some micron and submicron porosity remains present (Figure 6b). Submicron porosity is particularly prevalent in areas with higher W content (indicated in micrographs by lighter Z-contrast). These areas can also show $FeWO_4$ whisker formation (Figure 6d), consistent with chemical vapor transport being active during oxidation.[48,49] With continued cycling, CVT may be responsible for a small amount of mass loss from the foam, measured as ≈1 mg per cycle for a Fe-25 at.%W (Fe-52 wt.% W)foam with 800 mg starting mass; this material condenses onto the sides of the furnace tube and the insulating block during cycling. Analysis of the insulating block and tube inner surface showed significant Fe content as well, indicating that the mass loss measured may instead be due to the mechanical spalling of powders during cycling. In either case, although the lost mass is no longer in the foam, it is still redox-active and will continue cycling as long as it remains at an elevated temperature.

Redox cycling again induces homogenization of pore size, pore distribution, and phase distribution within the lamellae. After ten cycles, the reduced state shows a more even distribution of Fe_2W, and proliferation of submicron CVT pores. The ten cycles oxidized state shows that these pores are still largely filled during oxidation, and $FeWO_4$ whiskers are prevalent in some areas, as seen in Figure 6d (green arrow). At 20 cycles in the reduced state, more submicron pores are observed, and the lamellar surface continues to undergo homogenization: rather than a flat Fe sheet dotted with Fe_2W grains, the pore homogenization transforms the surface into a 3-D interconnected web of micron-scale Fe ligaments which are prevented from coarsening with each other by Fe_2W interconnects. At 20 cycles in the oxidized state, significant porosity is present after oxidation, and the oxidized microstructure is similar to the reduced microstructure, except for partial filling of the pores due to the volumetric expansion: the micro-scale pores remain largely visible, though the submicron pores are filled. At 50 cycles, the reduced and oxidized microstructure are again similar, showing little change from the 20-cycle state. Some whiskers are still observed in the oxidized state, though they are less prevalent than in earlier cycles. A net decrease in the size of the $FeWO_4$ regions is observed as well, from ≈5 µm at one cycle to ≈2 µm at ten cycles, to <1 µm at 20 cycles and beyond (green arrows). Finally, at 100 cycles, the microscale porosity has expanded, while the submicron pores remain intact, with no evidence of degradation as compared to the 50-cycle foam.

XRD diffraction patterns of the foams in the reduced state at 1, 10, 20, 50, and 100 cycles, shown in **Figure 7a**, reveal that the phase composition in the reduced state is not changed with cycling and that the Fe_2W XRD pattern contains both a broad (103) peak at $2\theta = 40–45°$ (indicative of nanocrystalline structure) and a sharp (110) peak at $2\theta = 38°$. The (200), (112), and (201) peaks at $2\theta = 44.3$, 45, and 45.9°, respectively, are difficult to characterize as crystalline or nanocrystalline due to their proximity to each other and to the Fe peak at $2\theta = 45.2°$: they fall in the shaded region in Figure 7a. This coexistence of both crystalline and nanocrystalline peaks in the same diffraction pattern is observed at all cycling points and was also previously observed in our study of Fe-25Mo and by Morales et al. in a study of MoO_3 reduction by hydrogen.[26,50] The similarity of the pattern observed here to the Fe_2Mo pattern observed by Morales et al. indicates that the (112) peak observed here is likely crystalline rather than nanocrystalline as well.[50] The oxidized state diffraction patterns (Figure 7b) show crystalline character for both Fe_3O_4 and $FeWO_4$, and the diffraction patterns do not change during cycling, indicative of stable phase evolution and consistent oxidation of both phases.

2.4. Architecture Evolution of Freeze Cast Foams

While the microstructure shows remarkable steadiness, the overall architecture deforms significantly during cycling due to the buckling of the Fe-25 W lamellae. Due to their high aspect ratio, lamellae are easily deformed in the metallic, reduced state, as the expansion and contraction of cycling induce significant stress within the lamellae. These stresses develop because each lamella is constrained by neighboring colonies. Additionally, the high operating temperature lowers the yield stress of the metal, resulting in plastic deformation at lower stresses, as well as creep deformation which can result in additional deformation over long cycling times. The reduced, metallic state is expected to be relatively prone to plastic buckling due to the high porosity of the lamellae.

Because the W-containing compounds effectively prevent sintering entirely in the foam, the buckling damage accumulates without the sintering of neighboring lamellae. As a result, as shown in **Figure 8**, the foams exhibit severe lamellar buckling in both axial and radial directions. This deformation frequently

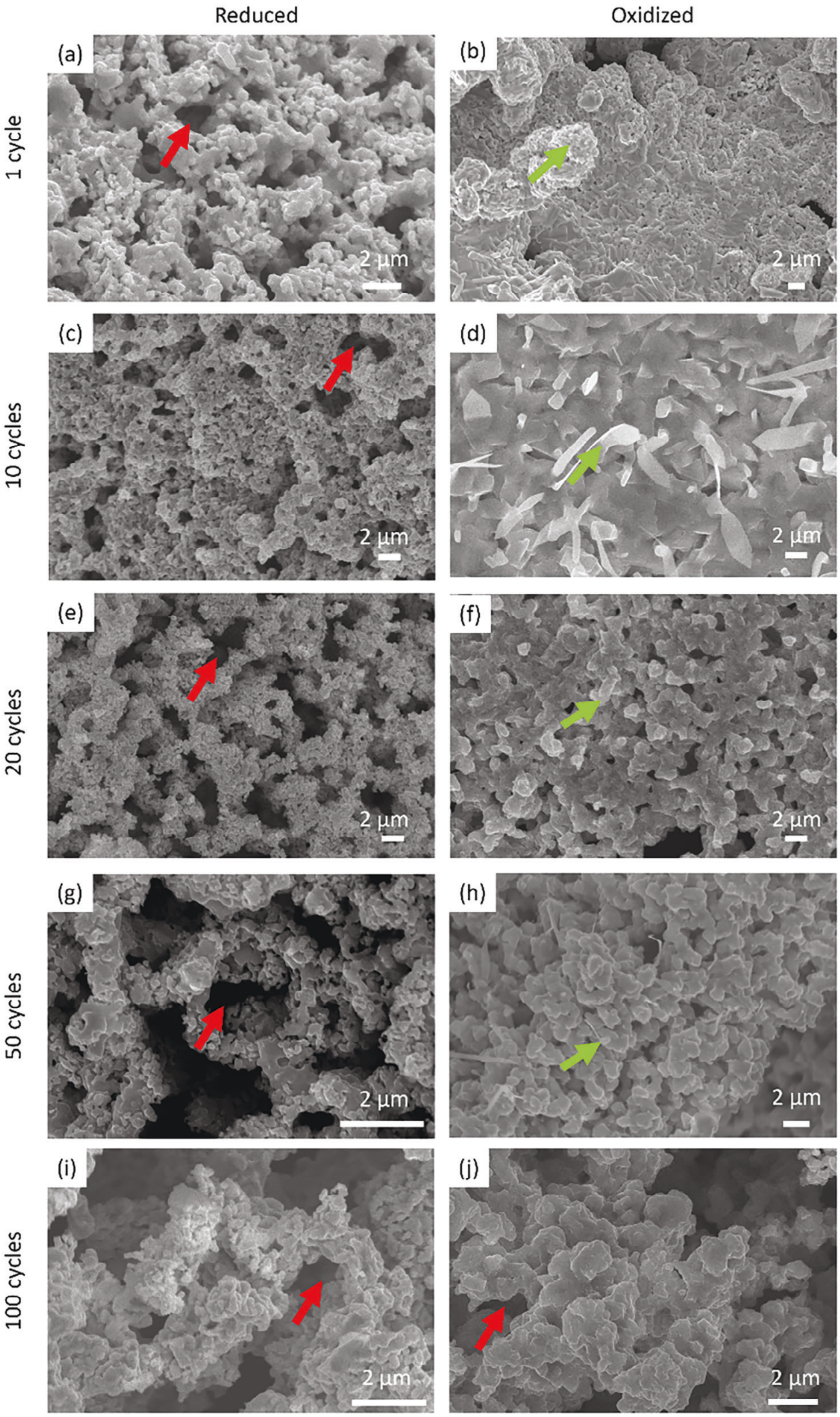

Figure 6. Surface SEM micrographs of Fe-25 W lamellae after 1, 10, 20, 50, and 100 redox cycles in the reduced state (left column) and the oxidized state (right column). Red arrows mark micropores and green arrows mark W-rich features.

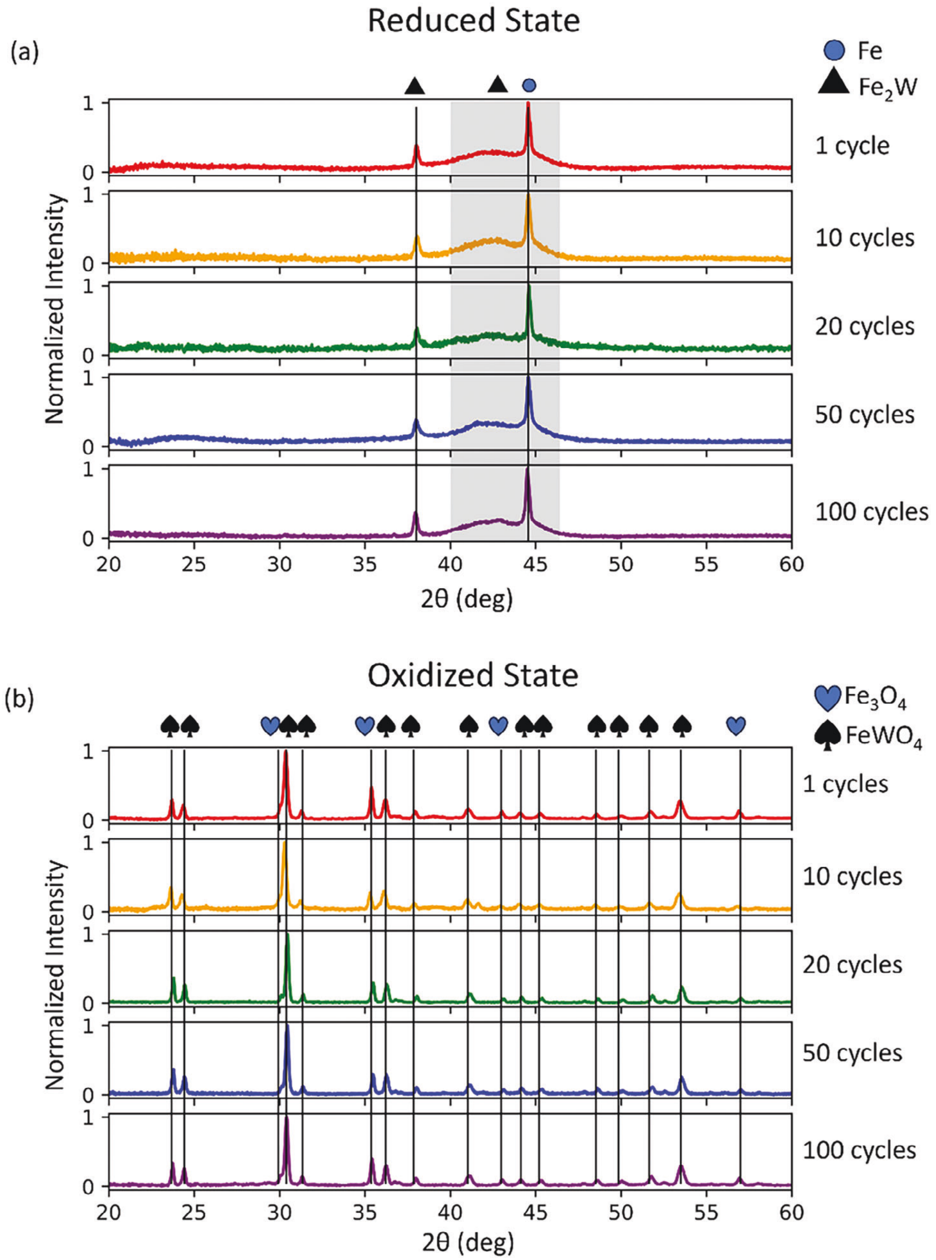

Figure 7. XRD spectra taken from polished cross-sections of a) reduced foams after 1, 10, 20, 50, and 100 cycles, with Fe and Fe_2W peak positions indicated. The shaded gray region indicates the diffraction angle range where Fe_2W peaks show nanocrystalline broadening, causing convolution with other peaks. b) oxidized foams after 0, 10, 20, 50, and 100 cycles, with Fe_3O_4 and $FeWO_4$ peak positions indicated.

leads to the formation of buckled bundles, characteristic of buckling of thin objects.[51]

The axial buckling is least severe at the top of the foam and grows in amplitude toward the bottom of the foam, resulting in a characteristic brooming deformation (Figure 8, blue dashed lines). This shape may be explained by either gravity or the expansion of the foam against the underlying alumina plate causing buckling along the axial direction. The lower side of the foam, while still porous, loses the directional porosity initially present from freeze casting.

The severe plastic buckling does not reduce the redox reactivity of the foam, though it can result in increased tortuosity and loss of macroporosity, particularly at the center of the foam where many buckled lamellae meet, resulting in a loss of the original directional porosity (Figure 8, red circle).

2.5. Micro- and Macrostructure Evolution of Powder Beds

The excellent resistance against degradation inherent to the Fe-25 W microstructure and the continued performance of the

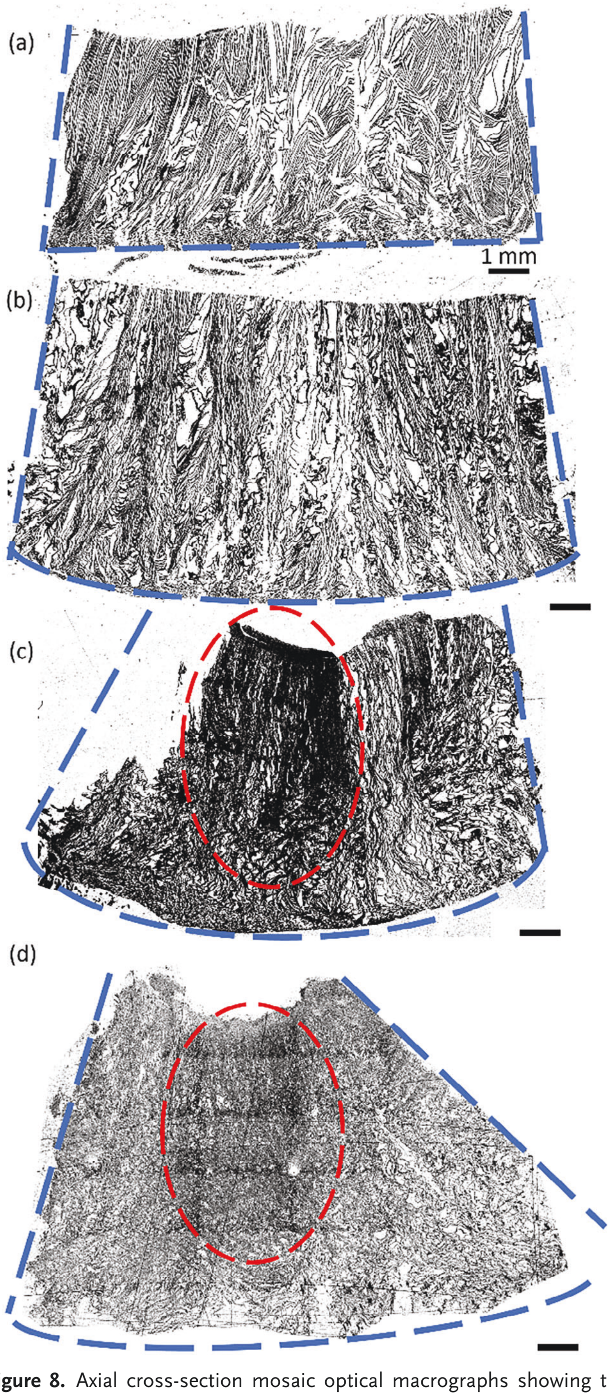

Figure 8. Axial cross-section mosaic optical macrographs showing the evolution of lamellar architecture after 1, 10, 20, and 50 redox cycles. Blue dashed lines indicate the foam envelope volume, red circle indicates a region at the center of the foam where the lamellar structure is no longer present.

freeze-cast foams (even after undergoing severe buckling and shape change) both question whether similar performance can be achieved from a packed powder bed with without a lamellar architecture. Surface and cross-section micrographs of reduced powder beds after 1, 10, 20, 50, and 100 cycles are shown in **Figure 9**.

The microstructure is identical to that of the freeze-cast foams, with the same micron- and submicron porosity observed throughout the foam. The Fe ligaments decorated with Fe_2W nanograins are observed as well, and they exhibit the same structural characteristics as in the freeze-cast foams. Furthermore, the redox cycling induces homogenization in the powder bed (as in the foams), even from a relatively coarse starting state; the initially micron-size domains of the Fe_2W phase (Figure 9a, green arrows) are fragmented into submicron domains (red arrows) interrupted by submicron pores after ten cycles, and the structure remains well homogenized afterward, with high porosity and reactivity due to the micron- and submicron porosity networks present. The macroporosity differs however: the packed beds have a much higher tortuosity, with no structured channels for gas ingress and egress built into the architecture, and with a lower initial porosity of 78% (vs 92% for the freeze-cast foams). Some larger channels exist, however, due to the agglomeration of different regions during packing. With continued redox cycling, the bed porosity increases, resulting in easier gas access to all parts of the bed.

3. Conclusion

A very high resistance against degradation is observed in Fe-25 W (at%) freeze-cast lamellar foams undergoing steam-hydrogen redox cycling at 800 °C. This resistance is attributed to the inhibition of sintering provided by W, as well as to the phase evolution of the Fe-25 W system. Tungsten is always found atomically mixed with Fe, either in the intermetallic λ–Fe_2W or in the mixed oxide $FeWO_4$ phases. This effectively prevents W from segregating into a pure W phase that would reduce the degradation resistance of the foam, as observed for Mo in the Fe-25Mo system.[26,52]

The lasting redox reactivity of the foam also depends upon its hierarchical porous architecture: i) macroscopic freeze-cast channels with low tortuosity, allowing easy gas access into, and out of, the foam, ii) microscale sintering inhibition pores, fully interconnected, which increase the surface area (and thus reactivity) of each lamella, and iii) submicron chemical-vapor-transport pores, regenerated at each reduction half cycle, which greatly increase surface area and limit damage accumulation by effectively reestablishing the original microstructure after each cycle, producing nanocrystalline λ–Fe_2W with corresponding nanopores. This microstructural stability allows for each lamella to grow progressively more porous (rather than denser) with cycling, with the W-rich phases becoming both smaller in morphology and more homogeneously distributed throughout the lamellae, increasing the sintering inhibition effect and generating more submicron pores to accelerate subsequent reaction.

During redox cycling, the lamellar structure gradually degrades into a less directional morphology, as neighboring lamellae buckle and contact each other. Unlike previously studied Fe-X systems, however, this does not impact the overall reactivity of the foams, as the microscale and submicron pore networks remain intact. Cycling of powder beds shows similar characteristics to directional freeze-cast foams, indicating that, for the Fe-25 W system, directional porosity is not necessary for long-term cycling stability.

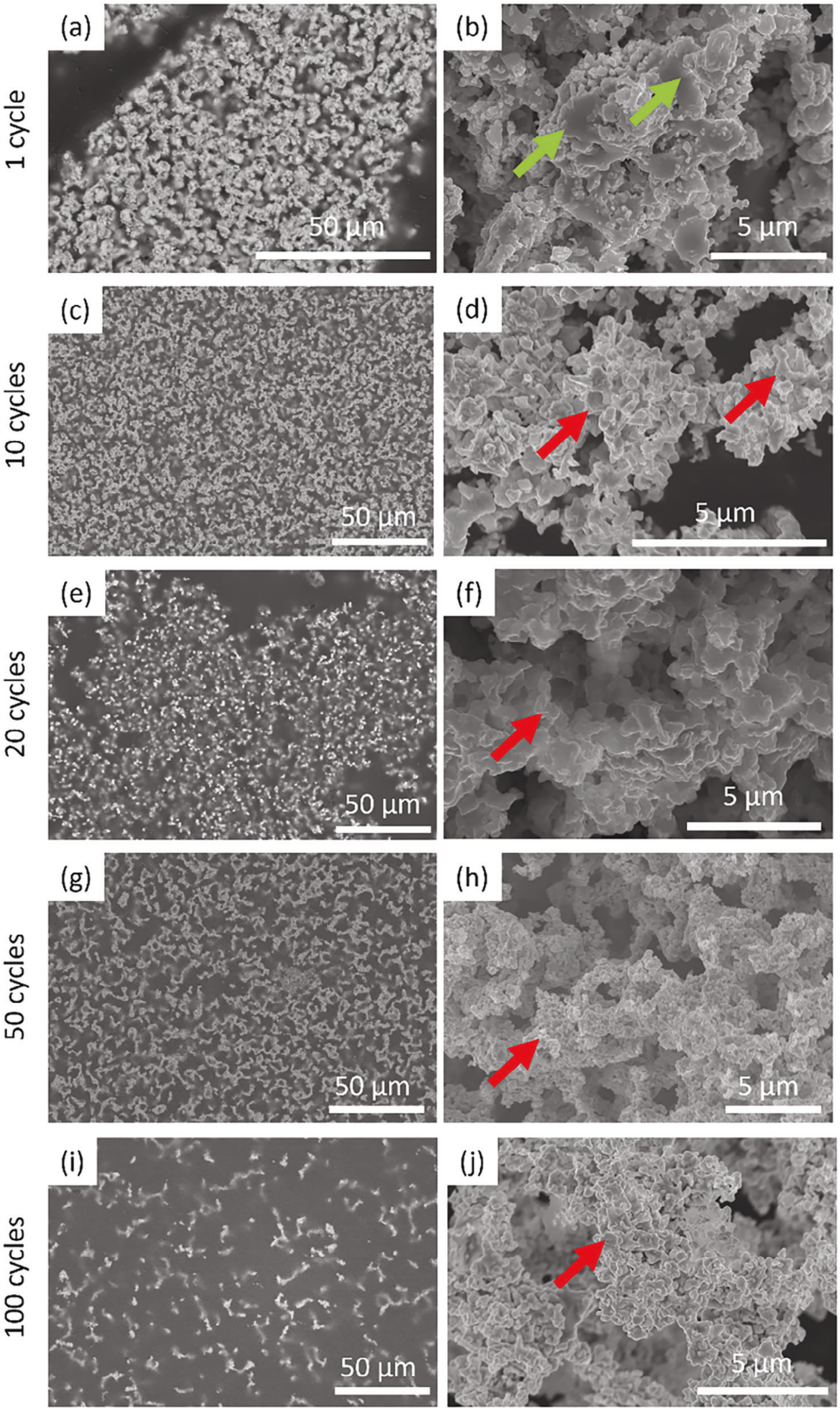

Figure 9. Axial cross-sectional SEM micrographs (left) and surface micrographs (right) of Fe-25 W tapped powder beds in the reduced state after a,b) one cycle, c, d) ten cycles, e,f) 20 cycles, g,h) 50 cycles, and i,j) 100 cycles. Green arrows point to a relatively large initial Fe grain size, which shrinks to submicron (red arrows) with cycling.

4. Experimental Section

Foam Fabrication: Fe-25 W (at%) freeze-cast foams were prepared by aqueous freeze casting, following procedures developed in previous work for Fe—Ni, —Co, —Cu and —Mo foams.[19,24,26,30,33,53] An aqueous slurry was prepared, containing 5.84 vol% Fe_2O_3 (Noah Technologies, 99.9%, <3 µm), 4.15 vol% WO_3 (SSNano, 99.5%, <100 nm) and 87.46 vol% DI water. By mass, the Fe_2O_3/WO_3 ratio is 0.965. Additionally, 0.55 vol% Zephrym PD 4974 (Croda) was added as a dispersant. This slurry was ball-milled for 24 h with yttria-stabilized zirconia milling media on a rotary ball mill. After milling, 2.00 vol% polyethylene glycol was added as a binder. The prepared slurry was degassed and then chilled to 0 °C in an ice bath before freeze-casting.

Directional freeze casting was performed on a copper plate chilled by a thermoelectric cooler (Mauser). The slurry was poured into a Teflon mold (25 mm OD, 15 mm ID, 15 mm height) and the temperature of the copper base of the plate was reduced to −30 °C following an exponential cooling curve; this cooling profile yields a constant rate of ice growth such that the formed lamellae maintain a constant thickness and spacing throughout the height of the foam.[54] After freeze casting, the lowest 1 mm of the frozen foam was removed by razor blade. The cast foams were freeze-dried (0.13 mbar residual pressure) for 24 h at −54 °C to remove all ice before further processing.

After freeze drying, the oxide green bodies were heat treated to yield metallic foams. First, the organic material was burnt out at 300 °C for 1 h, then the oxides were reduced with H_2 at 600 °C for 4 h, and finally, the foams were sintered at 1200 °C for 3 h (10 °C min^{-1} heating and 5 °C min^{-1} cooling rates throughout) under flowing H_2 (UHP, Airgas). The average foam mass after reduction and sintering was 0.83 g.

To prepare tapped powder beds for comparison, the slurry was prepared as described above for the freeze-cast foams; it was then dried in laboratory air for 72 h rather than freeze-cast, and then ground to powder by hand with a mortar and pestle. The same heat treatment as for the freeze-cast foams was used on these powders, which were kept in an alumina tube (9 mm ID) to maintain a cylindrical shape while in the furnace.

Foam Redox Cycling: Redox cycling was carried out in an alumina tube furnace (20 mm ID, 500 mm length) at 800 °C (10 °C min^{-1} heating rate) fed by both H_2 and H_2O. Pure H_2 (UHP, Airgas) was delivered directly by a mass flow controller at 200 sccm. Steam (H_2O) was delivered by flowing Ar (UHP, Airgas) as a carrier gas at 120 sccm through bubbling in water heated to 93 °C (to provide an H_2O pressure of 770 mbar, sufficient to oxidize Fe to Fe_3O_4).[55] Alternating cycles of H_2 and H_2O exposure, 90 min each, were controlled by a LabVIEW program. The gas used during cooldown was either 100 sccm H_2 (for foams in the reduced state) or 20 sccm Ar-4% H_2 (for foams in the oxidized state). A cooling rate of 5 °C min^{-1} was used, and the foams were brought to room temperature before removing from the furnace. The freeze cast foams were unconstrained, and thus free to expand and contract during the redox cycles. For the powder beds, two sample sets were fabricated: one set was taken out of the alumina tube (9 mm diameter) and was free to expand and contract like the freeze-cast foams, and the other set was left in the alumina tube throughout the cycling, thus being radially constrained.

Foam Microstructural Characterization: To obtain cross-sections, foams were mounted in epoxy and vacuum infiltrated to fill pores before grinding and polishing to 1 µm. The mounted foams were then ion-milled with a Leica TIC3X to improve surface visibility. Polished samples were sputter-coated with 9 nm Au/Pd for SEM characterization. SEM characterization was performed on Hitachi SU8030 on either unmounted foams (with as-fabricated surfaces) or mounted and polished foam cross-sections.

X-Ray Characterization: In situ X-ray diffraction spectra recorded during redox cycling of freeze-cast specimens were collected in a similar setup to the previous work, with minor modifications.[24,30] Spectra were collected on a Stadi-MP (Stoe, Germany) instrument, with an asymmetric curved Ge monochromator under pure Ag-$K_{\alpha 1}$ radiation ($\lambda = 0.56$ Å) and a 1D silicon strip-detector (MYTHEN2 1k, from Dectris, Switzerland), operated at 40 kV and 40 mA (Beam Size 4 × 0.8 mm). Data were collected in Debye–Scherrer (transmission) geometry, using 1-min scans with 2θ diffraction angles spanning 5.7–24.3°, after calibration against a NIST Si standard (640d). A colony of metallic lamellae was extracted, using a razor blade, from a reduced and sintered Fe-25 W foam, measuring 1–1.5 mm in height and 1–1.5 mm in thickness. The lamellae were introduced in a 1.5 mm diameter quartz capillary and surrounded on both ends by amorphous quartz wool. The remainder of the capillary volume on the outlet end of the sample was filled with porous ceramic blocks to prevent sample movement upon changes in gas flow. The capillary was installed into a water-cooled, graphite-heated furnace, with a temperature stability of 0.1 °C.

The experiment began by heating the sample to 800 °C (30 °C min^{-1}) under flowing Ar-4% H_2, to ensure the sample remained metallic until the cycling temperature was reached. Once at 800 °C, the gas was switched to Ar, and bubbled through a 40 °C water bubbler ($P_{H2O} = 73$ mbar) for oxidation. All gas lines between the bubbler and capillary were heated to >40 °C to prevent steam condensation. Following complete oxidation, noted by unchanging diffraction patterns, Ar-4% H_2 flowed for reduction. This diluted reduction gas was used to slow the reduction reaction to match the time resolution of the data collection. This procedure was repeated for two consecutive oxidation-reduction cycles. Processing of diffraction patterns was done in Python, with waterfall plots of diffraction spectra, after background correction with a modified polynomial fit. For each phase of interest, the strongest diffraction peak, indexed using reference patterns from the Inorganic Crystal Structure Database (ICSD), was fitted to a Pseudo–Gaussian model using the lmfit package. These fitted peaks were then integrated to achieve an area, assumed to be proportional to the volume of the diffracting phase, and then normalized to the respective maxima of each phase.

Ex situ X-ray diffraction spectra were gathered in reflection mode from polished cross-sections on a Rigaku Smartlab Gen 2 with a Cu source. Data processing was performed in OriginLab to remove the epoxy background signal from the XRD spectra.

The thermodynamic analysis of the Fe-25 W system was performed using the energy and enthalpy of formation values experimentally measured for Fe_2W and $FeWO_4$, from Refs. [38–40] as well as standard values for Fe_3O_4 and H_2O from the NIST-JANAF thermochemical tables, following a standard procedure such as that described in Ref. [56] The equations used are described in the Supporting Information.

Supporting Information

Supporting Information is available from the Wiley Online Library or from the author.

Acknowledgements

This research was funded by the US National Science Foundation under grant CMMI-2015641. Experiments and characterization made use of the Materials Characterization and Imaging Facility, the NUANCE Center, the Jerome B. Cohen X-Ray Diffraction Facility (supported by SHyNE under NSF ECCS-1542205, MRSEC under NSF DMR-1720139, the International Institute for Nanotechnology, the Keck Foundation, and the State of Illinois), and the IMSERC X-Ray facility (supported by SHyNE under NSF ECCS-2025633) at Northwestern University (NU).

Conflict of Interest

DCD discloses a financial interest in CellMobility, Inc. which commercializes freeze-cast metal foams. DCD and SMP disclose patent applications for “Refractory Alloyed Iron-based redox active foams for Iron-Air Batteries”, U.S. Provisional Patent Application No. 63/406320, and “Iron-Tungsten Redox System and Applications of Same”, U.S. Provisional Patent Application No. 63/619.401.

Data Availability Statement

The data that support the findings of this study are available from the corresponding author upon reasonable request.

Keywords

chemical looping, energy storage, freeze casting, redox cycling, sintering inhibition

Received: March 20, 2024
Revised: April 16, 2024
Published online: May 1, 2024

[1] X. Zhao, N. Xu, X. Li, Y. Gong, K. Huang, *ECS Trans.* **2013**, *50*, 115.
[2] S. Trocino, M. Lo Faro, S. C. Zignani, V. Antonucci, A. S. Arico, *Appl. Energy* **2019**, *233*, 386.
[3] T. Mattisson, A. Lyngfelt, P. Cho, *Fuel* **2001**, *80*, 1953.
[4] T. Mattisson, M. Johansson, A. Lyngfelt, *Energy Fuels* **2004**, *18*, 628.
[5] I. S. Metcalfe, B. Ray, C. Dejoie, W. Hu, C. de Leeuwe, C. Dueso, F. R. García-García, C.-M. Mak, E. I. Papaioannou, C. R. Thompson, *Nat. Chem.* **2019**, *11*, 638.
[6] A. Thursfield, A. Murugan, R. Franca, I. S. Metcalfe, *Energy Environ. Sci.* **2012**, *5*, 7421.
[7] N. V. R. A. Dharanipragada, L. C. Buelens, H. Poelman, E. De Grave, V. V. Galvita, G. B. Marin, *J. Mater. Chem. A* **2015**, *3*, 16251.
[8] V. Galvita, T. Hempel, H. Lorenz, L. K. Rihko-Struckmann, K. Sundmacher, *Ind. Eng. Chem. Res.* **2008**, *47*, 303.
[9] M. Bui, C. S. Adjiman, A. Bardow, E. J. Anthony, A. Boston, S. Brown, P. S. Fennell, S. Fuss, A. Galindo, L. A. Hackett, J. P. Hallett, H. J. Herzog, G. Jackson, J. Kemper, S. Krevor, G. C. Maitland, M. Matuszewski, I. S. Metcalfe, C. Petit, G. Puxty, J. Reimer, D. M. Reiner, E. S. Rubin, S. A. Scott, N. Shah, B. Smit, J. P. M. Trusler, P. Webley, J. Wilcox, N. Mac Dowell, *Energy Environ. Sci.* **2018**, *11*, 1062.
[10] X. Han, L. Wang, Z. Ge, X. Lin, Y. Liu, S. Zhang, Z. Zuo, H. Chen, *Sol. Energy Mater. Sol. Cells* **2023**, *260*, 112475.
[11] M. E. Gálvez, P. G. Loutzenhiser, I. Hischier, A. Steinfeld, *Energy Fuels* **2008**, *22*, 3544.
[12] C. M. Berger, O. Tokariev, P. Orzessek, A. Hospach, Q. Fang, M. Bram, W. J. Quadakkers, N. H. Menzler, H. P. Buchkremer, *J. Energy Storage* **2015**, *1*, 54.
[13] C. D. Bohn, J. P. Cleeton, C. R. Müller, S. Y. Chuang, S. A. Scott, J. S. Dennis, *Energy Fuels* **2010**, *24*, 4025.
[14] X. Zhao, Y. Gong, X. Li, N. Xu, K. Huang, *J. Electrochem. Soc.* **2013**, *160*, A1716.
[15] P. Gayán, M. A. Pans, M. Ortiz, A. Abad, L. F. de Diego, F. García-Labiano, J. Adánez, *Fuel Process. Technol.* **2012**, *96*, 37.
[16] S. Ma, S. Chen, A. Soomro, W. Xiang, *Energy Fuels* **2017**, *31*, 8001.
[17] Q. Zafar, T. Mattisson, B. Gevert, *Energy Fuels* **2006**, *20*, 34.
[18] S. Wang, G. Wang, F. Jiang, M. Luo, H. Li, *Energy Environ. Sci.* **2010**, *3*, 1353.
[19] S. K. Wilke, R. A. Lundberg, D. C. Dunand, *ACS Appl. Mater. Interfaces* **2020**, *12*, 27190.
[20] C. Chung, L. Qin, V. Shah, L.-S. Fan, *Energy Environ. Sci.* **2017**, *10*, 2318.
[21] L. Zeng, Z. Cheng, J. A. Fan, L.-S. Fan, J. Gong, *Nat. Rev. Chem.* **2018**, *2*, 349.
[22] K. Otsuka, T. Kaburagi, C. Yamada, S. Takenaka, *J. Power Sources* **2003**, *122*, 111.
[23] M. Hasegawa, *Ellingham Diagram, Treatise on Process Metallurgy*, Elsevier, Amsterdam **2014**, pp. 507–516.
[24] J. B. Mack, S. M. Pennell, D. C. Dunand, *Acta Mater.* **2022**, *237*, 118148.
[25] A. Ruiz Puigdollers, P. Schlexer, S. Tosoni, G. Pacchioni, *ACS Catal.* **2017**, *7*, 6493.
[26] J. B. Mack, S. M. Pennell, D. C. Dunand, *Acta Mater.* **2023**, *254*, 119015.
[27] W. V. Schulmeyer, H. M. Ortner, *Int. J. Refract. Metals Hard Mater.* **2002**, *20*, 261.
[28] J. J. Morales Corona, K. Sedransk Campbell, P. S. Fennell, *Sci. Technol.* **2023**, *13*, 565.
[29] R. Liu, C. Pei, X. Zhang, S. Chen, H. Li, L. Zeng, R. Mu, J. Gong, *Chin. J. Catal.* **2020**, *41*, 1140.
[30] S. M. Pennell, J. B. Mack, D. C. Dunand, *J. Alloys Compd.* **2022**, *918*, 165606.
[31] S. M. Pennell, B. Chappuis, J. A. Carpenter, D. C. Dunand, *Adv. Funct. Mater.* **2023**, *33*, 2307470.
[32] A. A. Plunk, D. C. Dunand, *Mater. Lett.* **2017**, *191*, 112.
[33] S. K. Wilke, D. C. Dunand, *Acta Mater.* **2019**, *162*, 90.
[34] S. K. Wilke, D. C. Dunand, *J. Power Sources* **2020**, *448*, 227463.
[35] S. Deville, *J. Mater. Res.* **2013**, *28*, 2202.
[36] K. L. Scotti, D. C. Dunand, *Prog. Mater. Sci.* **2018**, *94*, 243.
[37] W. Zhang, J. Zhang, Q. Li, Y. He, B. Tang, M. Li, Z. Zhang, Z. Zou, Thermodynamic analyses of iron oxides redox reactions, Proceedings of the 8 th Pacific Rim International Congress on Advanced Materials and Processing, Springer, Berlin, Heidelberg **2016**, pp. 777–789.
[38] J. Amosse, J. C. Mathieu, *J. Chem. Thermodyn.* **1980**, *12*, 683.
[39] T. Rezukhina, T. Kashina, *J. Chem. Thermodyn.* **1976**, *8*, 519.
[40] N. G. Schmahl, H. Dillenburg, *Z. Phys. Chem.* **1972**, *77*, 113.
[41] C. Zhang, K. Huang, *Adv. Energy Mater.* **2021**, *11*, 2000630.
[42] Y. Ma, I. R. Souza Filho, Y. Bai, J. Schenk, F. Patisson, A. Beck, J. A. van Bokhoven, M. G. Willinger, K. Li, D. Xie, D. Ponge, S. Zaefferer, B. Gault, J. R. Mianroodi, D. Raabe, *Scr. Mater.* **2022**, *213*, 114571.
[43] D. Spreitzer, J. Schenk, *Steel Res. Int.* **2019**, *90*, 1900108.
[44] A. Habermann, F. Winter, H. Hofbauer, J. Zirngast, J. L. Schenk, *ISIJ Int.* **2000**, *40*, 935.
[45] J. A. Bustnes, *Metall. Mater. Trans. B* **1997**, *28*, 613.
[46] X. Wu, J. Luo, B. Lu, C. Xie, Z. Pi, M. Hu, T. Xu, G. Wu, Z. Yu, D. Yi, *Trans. Nonferrous Metals Soc. China* **2009**, *19*, s785.
[47] S. K. Wilke, D. C. Dunand, *J. Mater. Chem. A* **2020**, *8*, 19375.
[48] M. Sadeghi, S. Rezaee, A. Arman, Ş. Ţălu, C. Luna, R. Shakoury, *Mater. Res. Express* **2019**, *6*, 1265f7.
[49] S. Wang, Y. He, J. Zou, Y. Wang, H. Huang, *J. Alloys Compd.* **2009**, *482*, 61.
[50] R. Morales, D. Sichen, S. Seetharaman, I. Arvanitidis, *Metall. Mater. Trans. B* **2002**, *33*, 589.
[51] A. Guerra, A. C. Slim, D. P. Holmes, O. Kodio, *Phys. Rev. Lett.* **2023**, *130*, 148201.
[52] S. M. Pennell, B. Chappuis, J. A. Carpenter, D. C. Dunand, *Adv. Funct. Mater.* **2023**, *33*, 2307470.
[53] S. Pennell, D. Dunand, *Acta Mater.* **2022**, *243*, 118543.
[54] C. Stolze, T. Janoschka, U. S. Schubert, F. A. Müller, S. Flauder, *Adv. Engin. Mater.* **2016**, *18*, 111.
[55] I. G. Wright, R. B. Dooley, *Int. Mater. Rev.* **2010**, *55*, 129.
[56] R. O'hayre, S.-W. Cha, W. Colella, F. B. Prinz, *Fuel Cell Fundamentals*, John Wiley & Sons, Hoboken, NJ **2016**.